Landslides
DOI 10.1007/s10346-022-01899-3
Received: 24 January 2022
Accepted: 1 May 2022
© The Author(s) 2022

Margaret M. Darrow · Victoria A. Nelson · Michael Grilliot · Joseph Wartman · Aaron Jacobs · James F. Baichtal · Cindy Buxton

Geomorphology and initiation mechanisms of the 2020 Haines, Alaska landslide

Abstract In early December 2020, an atmospheric river (AR) and rain-on-snow (ROS) event impacted the Haines, Alaska area, resulting in record-breaking rainfall and snowmelt that caused flooding and dozens of mass movement events. We consider the AR—a one-in-500-year event—as the trigger for the devastating Beach Road Landslide (BRLS), which destroyed or damaged four residences and took the lives of two people. The BRLS started as a debris avalanche and transitioned into a debris flow, with a total approximate landslide volume of 187,100 m^3. Geomorphic analysis using lidar data identified evidence of paleo-landslides and displaced masses of rock, one of which served as the source area for the BRLS. Significant structural features in the weak ultramafic bedrock defined the head scarp area and formed the failure plane. This study illustrates the importance of identifying pre-existing landslide features and source areas likely to produce future landslides. As an increase in ROS events is projected for Southeast Alaska with warmer and wetter winters, we recommend the development of an AR scale coupled with geological information for the region, to enhance warnings to residents in landslide-prone areas.

Keywords Debris avalanche · Debris flow · Rain-on-snow · Landslide · Atmospheric river · Alaska

Introduction

In early December 2020, an atmospheric river (AR) hit Southeast Alaska, including the town of Haines. This AR event raised temperatures well above freezing, and delivered record-breaking rainfall. Much of the snowpack melted, which increased runoff volume, resulting in flooding and landslides that washed out roads, damaged utilities, and impacted homes. Although dozens of mass movement events occurred during or shortly after a two-day period of intense precipitation, here we focus on a devastating landslide along Beach Road (Fig. 1) that destroyed three residences and severely damaged a fourth, and took the lives of two occupants. The Beach Road Landslide (BRLS) occurred in an area thought to be safe by residents and community planners (Godinez 2020). Thus, at the time of the landslide, there were no landslide mitigation measures in place along Beach Road.

We explore the significant precipitation and rapid snowmelt from heavy rain-on-snow (ROS) produced by the AR as a potential trigger for the December 2020 BRLS. It is easier to produce runoff from a new, "ripening" snowpack—snow that is isothermal at 0 °C and ready to change phase from a solid to a liquid (Guthrie et al. 2010)—than from an older and colder snowpack. In ROS events, rain often falls on ripening snow, contributing to the overall runoff due to the storm (Brideau et al. 2012; Guthrie et al. 2010). Landslides triggered by ROS events have been studied in the western USA, Canada, Italy, and Japan (e.g., Ayalew et al. 2005; Brideau et al. 2012; Cacek 1989; Cardinali et al. 1999; Coe et al. 2016; Contreras et al. 2009; DeGraff 2001; Evans 2002; Naudet et al. 2008; Wisher 1998). In nearly all of these cases, heavy rainfall and snowmelt increased pore water pressure, causing reactivation of previous landslides or triggering new landslides in pre-existing landslide areas. To the best of our knowledge, no published studies document ROS-induced landslides in Alaska, although there is precedent for such events. For example, an AR impacted Southeast Alaska in November 2005, setting the historic record for rainfall in Haines and resulting in $4 million in damage throughout the region (Weather Bureau 2005). Although similar to the 2005 event, the December 2020 storm set new records and had more than twice the rainfall intensity, impacting far more people and their property. It is critical to understand precipitation-induced landslides in Alaska, which is experiencing the early effects of a rapidly changing climate (e.g., Larsen et al. 2008).

This paper seeks to answer the question, "Why did this devastating landslide occur here?" First, we summarize the extraordinary storm event of late 2020. We then present an analysis of the regional and local geology including soil properties and rock strength values, and detail a geomorphic analysis of the North Riley Ridge area (area of interest, AOI, in Fig. 2). Finally, we use multiple epochs of lidar data, including high-resolution lidar and imagery collected using un-crewed aerial systems (UAS) in 2021, to understand active slope processes in the BRLS area.

General study area

Haines is located in the northern part of Southeast Alaska, approximately 72 km from the US–Canada border at the south terminus of the Haines Highway (Fig. 2). The majority of the Haines community is located on a low-lying saddle between the Takshanuk Mountains to the northwest and the Chilkat Peninsula to the southeast. We focus our analysis on the AOI indicated in Fig. 2, which encompasses North Riley Ridge, Beach Road, and the 2020 BRLS.

Geological setting

Haines is located in the Wrangellia terrane (Brew and Ford 1994; Himmelberg and Loney 1995), which accreted to the North American continent during the Late Jurassic (Brew and Ford 1994). The area was covered by massive tholeiitic basalt flows and intruded by related gabbroic intrusive bodies during the Carnian Stage of

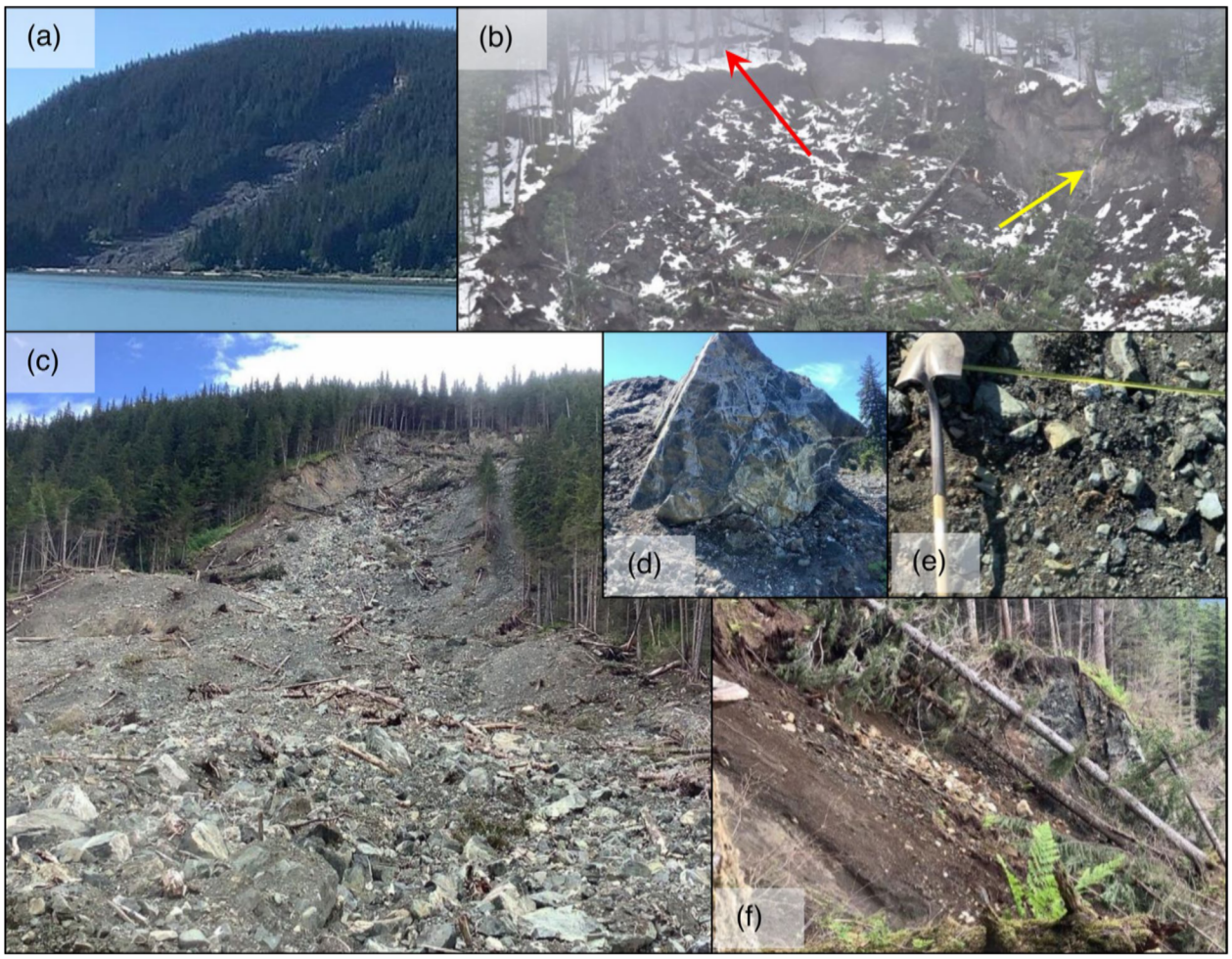

Fig. 1 Beach Road Landslide (BRLS): (**a**) view from Nukdik Point approximately 2.3 km to the NW (the city of Haines is to the right out of the photograph); (**b**) image of the head scarp area taken on December 8, 2020 (red arrow points to crack and yellow arrow points to waterfall; image by E. Stevens); (**c**) looking up towards the head scarp from the pioneer road across the landslide body; (**d**) ultramafic boulder (~5 m in diameter) on lower landslide body; (**e**) example of landslide matrix; (**f**) smooth joint surface exposed in the west to the central portion of the head scarp. All photographs except for (**b**) were taken in June 2021

the Upper Triassic (Brew and Ford 1994; Plafker et al. 1989). In the North Riley Ridge area, Davis and Plafker (1985) mapped the bedrock as mid-Cretaceous undifferentiated ultramafic rocks (108 m.y. based on potassium-argon dating; MacKevett et al. 1974), which intruded into the Upper Triassic basalt that composes most of the Chilkat Peninsula to the south. The mineralogy of the ultramafic unit varies between pyroxenites and hornblendites with highly variable and often significant amounts of magnetite and/or biotite. Himmelberg and Loney (1995) identified the bedrock in this area as clinopyroxenite, with varying amounts of hornblende, olivine, biotite, and magnetite.

Strands of the Denali Fault System (DFS) run to the west and east of the Haines area trending NW–SE, with the Chilkat River segment to the west, and the Chilkoot Inlet and Lutak Inlet faults to the east (Fig. 2; Brew and Ford 1994; Wilson et al. 2015). Brew and Ford (1994) inferred approximately 150 km of right-lateral separation on the Chilkoot Inlet-Lutak Inlet fault splay, active from the middle Tertiary into the Quaternary. The Chilkat River segment of the DFS transitions into the Chatham Strait fault south of the Chilkat Peninsula. Brothers et al. (2018) indicate that the Chatham Strait fault has been inactive for at least the last 14,000 years, and suggest that active movement has transitioned to faults to the west of the project area. A similar analysis has not been done on the faults bordering the Chilkat Peninsula.

During the Last Glacial Maximum (LGM), this region was blanketed by glaciers that coalesced to form the Cordilleran Ice Sheet (CIS; Manley and Kaufman 2002; Carrara et al. 2007; Kaufman et al. 2011), including a glacier that occupied Lynn Canal and scoured down to the bedrock surface (Brothers et al. 2018). The CIS began to retreat rapidly from the coastal areas between 17,000 and 15,000 yr BP (Lesnek et al. 2020). The removal of the glacial ice weight resulted in glacial isostatic adjustment (GIA) of the crust. Analysis of uplifted paleo-shorelines indicates that the area around Haines was ice free by 14,000 yr BP (Baichtal et al. 2021). By 10,870 yr BP, the first forests following deglaciation were established on the Chilkat Peninsula (Cwynar 1990).

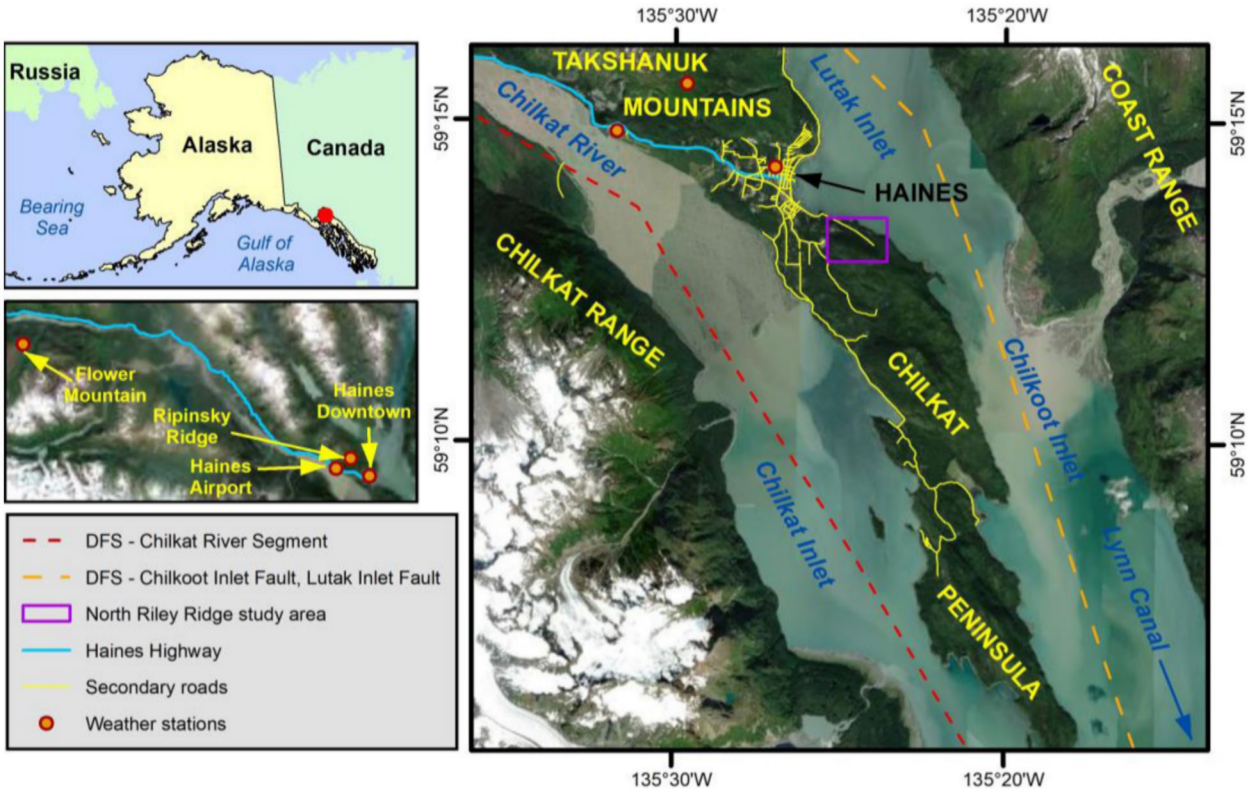

Fig. 2 Location of Haines, Alaska within the Lynn Canal region. Red point in the Alaska map inset identifies project location relative to Alaska and Canada. DFS is the Denali Fault System. Base map imagery from SOA (2021) and ADNR (2021); fault data modified from Wilson et al. (2015)

The Haines area currently experiences GIA due to loss of the ice formed during the Little Ice Age (LIA) in the Glacier Bay area to the west. The area began to rise around 1,770 AD, or approximately 250 years ago, with 4–4.5 m of uplift in the Haines area (Larsen et al. 2005). Current rates determined using global positioning system (GPS) geodetic techniques are as high as 20 mm/yr, and uplift is expected to continue for another several hundred years (Motyka et al. 2007). This uplift rate corresponds to that suggested by Lemke and Yehle (1972), who used tidal records from the early to the mid-twentieth century and determined a rate of 22.6 mm/yr. The retreating glaciers also left behind steep slopes that, around the project area, rise from sea level to ~ 354 m above sea level (asl) at slopes up to 88 degrees. Such slopes may be unstable due to oversteepening from glacial erosion and subsequent debuttressing from glacial ice (Evans and Clague 1999).

Climatic setting and December 2020 storm event

Southeast Alaska is well known for its wet weather. The renowned precipitation is due to frequent low-pressure systems collecting moisture as they travel across the North Pacific and end in the Gulf of Alaska (Baichtal et al. 2021; Kanan 2016). Haines is part of this maritime climate (Lemke and Yehle 1972; WRCC 2021). Records obtained from 2000 to 2019 from the Haines Downtown Cooperative Observer Program (COOP) station (AHNA2; N59.2381°, W135.4494°, 21.3 m) indicate average annual total precipitation and total snowfall amounts of approximately 160 cm and 464 cm, respectively (NWS 2021b). The mean annual temperature is 5.1 °C, with a record high of 31.7 °C and a record low of -24.4 °C (NWS 2021b; see Online Resource 1 for more information). Figure 3a contains a graphical summary of typical precipitation, snowfall, and snow depth.

As the 2020 AR moved into the Haines area on December 1, temperatures rose above freezing and well above the typical maximum values for the time of year (see Online Resource 1), resulting in rainfall rather than snowfall and causing the existing snowpack to melt. Using the AHNA2 station data, the greater-than-average snowpack dropped from 40.6 cm to 12.7 cm over the storm event (Fig. 3b). We converted this loss of snow to liquid water—or its snow water equivalent (SWE)—resulting in an additional 2.8 cm of water near sea level contributing to runoff. In December 2020, there was no weather station located on or near North Riley Ridge; anecdotally, however, roughly 1 m of snow was present on the ridge crest, which mostly melted during the AR event and may have contributed up to 10 cm of additional water to runoff. More evidence that points to significant changes in the snowpack is available from the Ripinsky Ridge Weather station (RRWA2; N59.2596°, W135.4942°, 793 m) and from the Flower Mountain SNOTEL site (1285; N59.4°, W136.278°, 765 m; see Fig. 2 for locations); data from these sites are contained in Fig. 3c and d, respectively. Approximately 150 cm of snow fell on Ripinsky Ridge over December 1 and 2, with two latter significant accumulations of 36 cm and 48 cm as additional storms moved

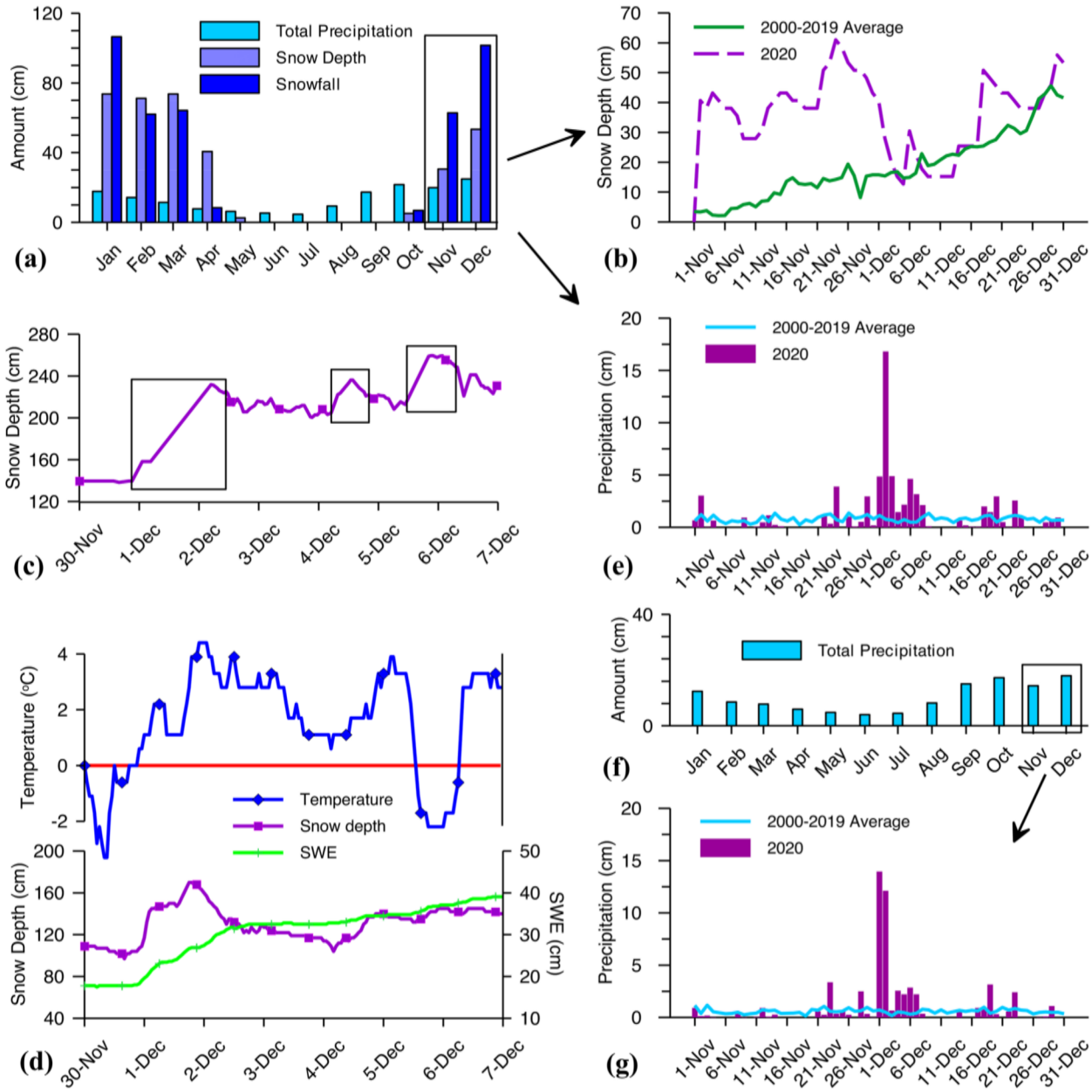

Fig. 3 Precipitation for Haines, Alaska: (**a**) monthly average total precipitation, snow depth and snowfall from 2000 to 2019 and (**b**) snow depth for 2020 compared to average values for November and December for the Haines Downtown COOP Station (AHNA2); (**c**) snow depth for Ripinsky Ridge Weather Station (RRWA2); (**d**) air temperature, snow depth, and snow water equivalent (SWE) for Flower Mountain Station (SNTL 1285); (**e**) daily precipitation totals for 2020 compared to average values for November and December for AHNA2. For the Haines Airport Station (PAHN), (**f**) monthly average total precipitation from 2000 to 2019 and (**g**) daily precipitation totals for 2020 compared to average values for November and December. Data from NWS (2021b), NWCC (2021), and MesoWest (2020)

through the area (Fig. 3c). At the Flower Mountain site (Fig. 3d), as temperatures climbed above 0 °C during the first 48 h of the AR event, the SWE increased by 14.7 cm with a loss of 40 cm of snow. This increase in SWE was from ROS and meltwater percolating through the snowpack. Due to this site's higher elevation, the snowpack was not ripe enough for runoff to make it to the ground surface. Closer to Haines, however, the ripening snowpack produced significant amounts of runoff through the duration of the event.

The rainfall produced by the 2020 AR was unprecedented in historic times. Figure 3e is a summary of both the average daily precipitation totals for November and December from 2000 to 2019, and daily precipitation totals just for 2020 for the AHNA2 station. On December 2, the precipitation received (16.8 cm) significantly exceeded the average value and broke the station's all-time daily precipitation record. The Haines Airport station (PAHN; N59.2473°, W135.5294°, 14.9 m) recorded similar averages from 2000 to 2019

(Fig. 3f). Using precipitation frequency estimates available for this station (NWS 2021a; Perica et al. 2012), the large 2-day total from December 1–2 (26.1 cm; Fig. 3g) represents a 500-year return interval (RI). After a brief respite from precipitation on December 3, moderate to heavy rain continued from December 4 to 7, as a series of weather fronts moved through the area. The longer duration (4–7 day) precipitation frequencies represented 50–200-year RI (NWS 2021a; Perica et al. 2012). It must be stressed that these RIs only account for the rainfall and not the runoff due to the melted snowpack; thus, the reported RIs are underestimates of the actual values (Brideau et al. 2012).

This tremendous amount of water manifested as increased groundwater pressures in the AOI, as demonstrated through anecdotal observations. For example, prior to the landslide on December 2, residents in a house near the BRLS discovered their toilet overflowing, presumably due to excess water pressure in the septic system. Additionally, an artesian well to the east of the landslide area that typically demonstrated a flow rate of 20–40 l min^{-1}, increased to 75–110 l min^{-1} after the storm events. Aside from these anecdotal observations, there were no other data on the water table in the North Riley Ridge area at the time of the landslide.

Geomorphology analysis of the North Riley Ridge study area

We used the slope map and contours derived from 2014 lidar data (QSI 2014) to map lineaments; paleo-landslide (PLS) head scarps, runout extents, and source areas; and paleo-shorelines (Fig. 4). All features were visually identified based on linear or arcuate patterns, changes in roughness, and breaks in contour lines. We mapped paleo-shorelines by identifying horizontal bench-like features, delineated at each bench's downhill slope break.

There are three major lineament sets in the study area, those running approximately NW–SE, N-S, and E-W (Fig. 4; see Online Resources 2 and 3 for additional information on average lineament trends). Based on their long persistence through the AOI, the lineaments are possibly faults that have been geomorphically enhanced and widened by glacial erosion. Multiple head scarps of PLS are evident in the lidar based on their concave shapes and steep headwalls. We also interpret the possible runout of three large PLS (Fig. 4) based on change in surface roughness and contour line breaks; approximate subaerial extents are provided in Table 1. Each of the inferred PLS extents may represent one landslide or be the accumulation of multiple events. Although the PLS may have run

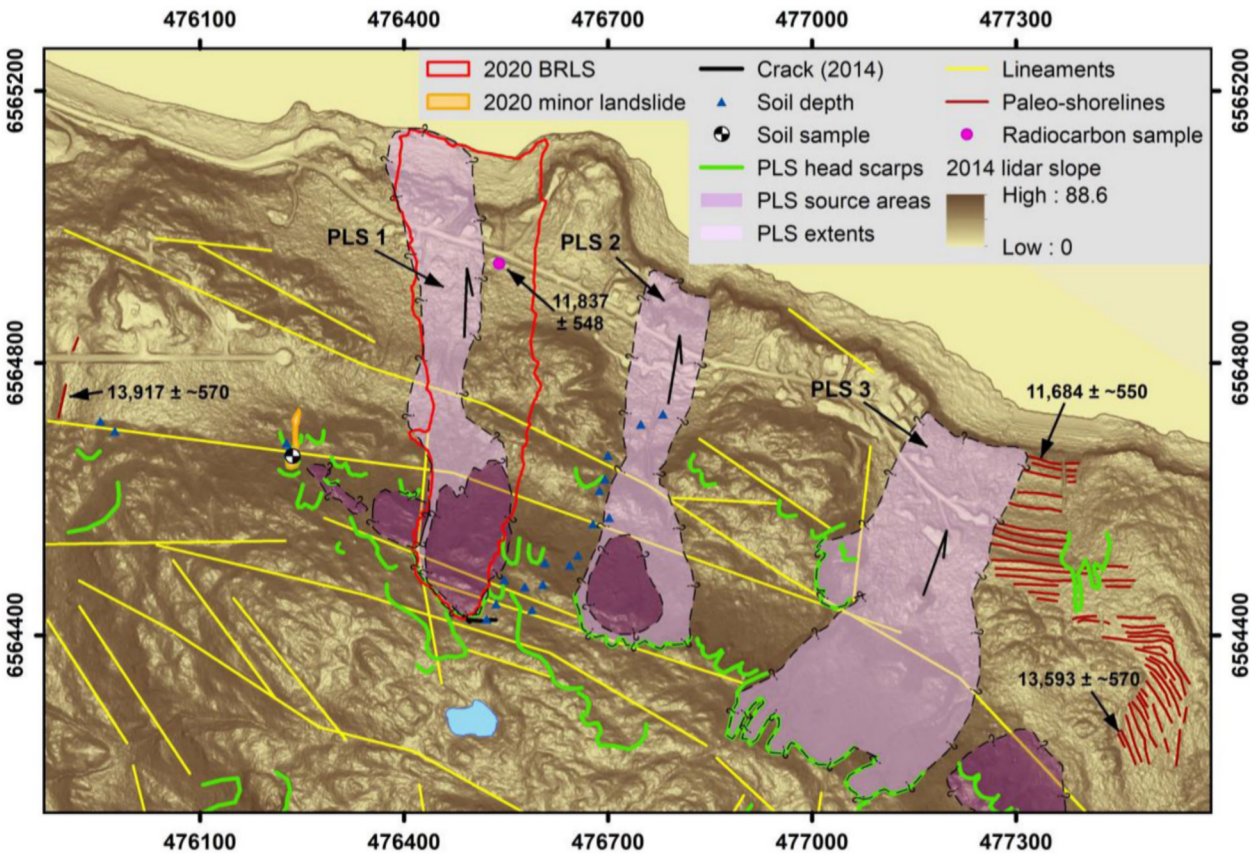

Fig. 4 Geomorphic interpretation of the AOI, including lineaments, paleo-shorelines, and paleo-landslide (PLS) extents, source areas, and head scarps. Dates of selected paleo-shorelines are provided. Map extents in UTM Z8. Base imagery is slope derived from 2014 lidar (QSI 2014)

Table 1 Paleo-landslide (PLS) interpreted approximate runout extents and source mass areas, as determined using 2014 lidar (QSI 2014); and age constraints based on paleo-shoreline ages

PLS	Runout extent ($\times 10^3$ m^2)	Source mass ($\times 10^3$ m^2)	Minimum age (yr BP)	Maximum age (yr BP)
PLS 1	76	20	--	--
PLS 2	63	11.6	250	--
PLS 3	127	Not identified	250	11,684 ± ~ 550

over topographic highs possibly consisting of competent bedrock (as was the case for the BRLS), we have constrained the inferred PLS extents to valleys. In the 2014 lidar, we mapped landslide source areas (term modified from Hungr et al.'s (2001) "landslide source volume") below several of the head scarps along North Riley Ridge, including below the head scarps for PLS 1 and 2 (Table 1). Each source area appears to be displaced material based on offset from the head scarp and the appearance of rotated blocks. It must be stressed, however, that the extents of both the PLS and the source areas are based on geomorphic interpretation and have not been confirmed with field investigations. There is precedent for large landslides occurring in Southeast Alaska following the LGM, as Baichtal et al. (2021) mapped landslides on the northeastern part of Chichagof Island (approximately 120 km south of the AOI) that both preceded and followed the maximum transgression associated with the LGM. Two other items of note visible in the 2014 lidar are a prominent crack extending to the east from the PLS 1 head scarp area, and a small pond near the ridge crest above the PLS 1 area (Fig. 4). In 2014, drainage from this pond flowed north, generally following a N-S trending lineament, and over the western portion of the PLS head scarp.

Paleo-shorelines are present throughout the greater Haines area, and prevalent in the eastern part of the AOI. These features form when the shore is exposed to wave action over a period of relative equilibrium. Recent work by Baichtal et al. (2021) and unpublished radiocarbon dates included here provide a correlation between the uplifted shoreline elevations and age. Online Resource 4 is a figure of radiocarbon dates of shell fragments and their corresponding elevations from the Haines area, as well as two approximations from Juneau, Alaska. The data also include shell fragments that were collected during the summer of 2021 in one of the borings made to install poles in the slide area to restore power to the Beach Road residents (see Fig. 4). Although there was no surface expression of a paleo-shoreline in this area preceding the 2020 BRLS, the type of shells and the sandy clayey matrix in which they were deposited suggest an intertidal environment; thus, their age is included in this analysis. These data indicate that ~ 110 m of uplift occurred within the AOI in approximately 4,000 years following the retreat of the valley glacier. These numbers point to an average uplift rate of ~ 27 mm/yr, similar to the rate of GIA that the Haines area is currently experiencing. Equation 1 is the inverse to the best-fit quadratic equation to the data in Online Resource 4:

$$Cal\ yr\ BP = 9900 + \sqrt{{}^{Elevation(m\ asl)}/_{6.6\times10^{-6}}} \quad (1)$$

This equation does not account for depression and subsequent GIA due to the LIA glacial advance, which may have modified beach deposits within ~ 5 m of current sea level (Larsen et al. 2005). Additionally, the Haines area experiences significant tides, with a high tide line 6.4 m above mean lower low water (Baichtal et al. 2021). As a result, wave action from the LIA or during subsequent rebound may have formed and/or modified any uplifted shorelines within ~ 10 m of mean sea level. Thus, we consider any uplifted shorelines with elevations between 0 and 10 m asl younger than 250 years, when rapid uplift of the area began (Larsen et al. 2005). For the uplifted beach deposits higher than 10 m asl, we applied Eq. 1 to the paleo-shoreline shapefile in ArcMap to calculate their approximate ages (see selected ages in Fig. 4). In addition to paleo-shorelines, a pronounced cliff beginning at 10 m asl, between 8 and 18 m high, and with a slope as high as 75°, is present along the entire northern shoreline within the AOI. Two possible origins of the cliff are 1) rapid uplift associated with a seismic event or 2) erosion due to wave action. Based on the lack of activity on the Chatham Strait fault (south of the AOI) for at least the last 14,000 years (Brothers et al. 2018), the terrace is more likely due to erosive wave action associated with the LIA glacial advance and related transgression.

The presence of paleo-shorelines in the area allows us to estimate the maximum age of PLS 3, which removed the surface expression of the paleo-shorelines from 60 to 21 m asl. The youngest of these is estimated to have formed 11,684 ± ~ 550 yr BP. The uplifted shorelines evident below the PLS 3 runout (not detailed in Fig. 4) provide a minimum age of 250 yr BP, making PLS 3 between 250 and ~ 11,000 years old (Table 1). Although no paleo-shorelines lie immediately adjacent to PLS 2, uplifted shorelines below its distal extent provide a minimum age of 250 yr BP. We did not identify any uplifted shorelines between the distal extent of PLS 1 and modern sea level; thus, there is no age control for this event. It must be stressed that the absence of paleo-shorelines does not always indicate their removal by a PLS. Instead, the presence of paleo-shorelines indicates areas where abundant source material was available for their formation.

December 2020 Beach Road Landslide (BRLS) event

The BRLS occurred at 1:17 pm on December 2 (Dryden, pers. comm., June 2021), as indicated by several people who heard the event. Residents recounted hearing a sound similar to a heavy explosion followed by a rumbling or scraping sound that lasted about 20–30 s; this was the first event of the BRLS. One resident thought it was a plow truck with the blade set too low and digging into the pavement. Topography muffled or reduced the sound depending on location, as some residents to the east and west of the slide along Beach Road did not hear it at all. Using Hungr et al.'s (2001) classification, the BRLS event began as a debris avalanche, and was soon after followed by a debris flow. The slide destroyed three residences in its path, sadly taking the lives of two residents. The slide flowed into the inlet causing a small wave that produced no damage. Although some of the debris from structures washed up on beaches

within several miles of the area, the vast majority of the impacted structures was swept into the inlet and remains undetected below the deposited landslide debris. This event also impacted adjacent properties, shifting one structure off its foundation and damaging or demolishing smaller out-buildings. After the first major event occurred, a resident captured some subsequent slide movement on mobile phone video. By comparing static features (such as boulders and trees) in the video to the June 2021 lidar data and high-resolution imagery, we approximated the movement velocity. After the initial debris avalanche event, the center of the debris flow traveled at 1.6 m s^{-1} (based on movement of a ~ 0.5-m-diameter rock relative to a static ~ 5-m-diameter boulder). Within a few minutes of the first event, a debris flood initiated along the east side of the landslide scar. Timing the movement of a tree transported in the flow, we estimate the debris flood's velocity at 5.5 m s^{-1}. Photographs of the landslide taken on December 8 captured a waterfall flowing over and down the western portion of the head scarp, approximately where the drainage from the uphill pond enters the area (see yellow arrow in Fig. 1b).

BRLS analysis

Some of the authors and personnel from the Alaska Division of Geological & Geophysical Surveys (DGGS) mobilized to Haines immediately following the landslide event in December 2020 to collect lidar data via a helicopter, and initial observations of the landslide body and head scarp area including structural measurements. In June 2021, the research team performed a reconnaissance of the area and collected 3D point cloud data using a Phoenix LiDAR Systems MiniRanger un-crewed laser scanner (ULS) and high-resolution imagery using a DJI Matrice 210 V2 RTK UAS. We deployed Leica GS18 Global Navigation Satellite System (GNSS) receivers for high-accuracy georeferencing and post-processing. This resulted in data with a ground resolution of 0.1 m for the lidar and 0.03 m for the high-resolution imagery. DGGS personnel collected sonar data of the seafloor immediately adjacent to the BRLS using a SR-Surveyor M1.8 with Edgetech 2205 540 kHz bathy/1600 kHz sidescan transducers. The research team also collected soil and rock samples, structural measurements of the bedrock, and soil depth measurements using a 1-m-long steel probe. Figure 4 contains locations of soil samples and depth measurements collected in the AOI, and Fig. 5a includes the locations of soil and rock samples.

Geometry, geology, and engineering properties

Based on interpretation of the June 2021 lidar data, the subaerial BRLS is approximately 687 m long and 170 m wide, covers 107,099 m^2, and has an overall slope angle of 20° but with local slope angles as high as 88° (Figs. 1a, c, 5a, b; see Online Resource 5 for longitudinal and cross-sectional profiles of the slide area). The landslide scoured down to bedrock in several areas, and deposited debris along both flanks, including piles of trees, rocks, and some debris from structures. The landslide surface consists of large boulders (up to 7 m in diameter; Fig. 1d) as well as a moist, slightly organic, non-plastic matrix of sand with gravel (Fig. 1e; summary of soil data in Online Resource 6). Soil depths averaged ~ 45 cm (22 measurements).

The rock component of the landslide body is representative of the bedrock outcrops present within and near the head scarp (Fig. 1f), along the lower right flank, and at the toe. The bedrock contains biotite, hornblende, and pyroxene crystals (0.5–3 cm), with a minor magnetite component; this is consistent with the biotite magnetite clinopyroxenite identification by Himmelberg and Loney (1995). For brevity, we will refer to this rock type as "ultramafic" (Fig. 1d). Hand samples easily separate along the biotite crystals. White diorite veins that intrude the ultramafic bedrock consist of quartz, plagioclase, hornblende, and biotite. Cobbles of diorite are also present within the landslide body, with a greater concentration to the east above the Beach Road alignment. We conducted point load strength index tests on diorite and ultramafic rock samples using a portable point load testing device (Wille Geotechnik); currently, we are limited to these strength data, as collecting samples for triaxial testing (for example) was beyond the scope of the initial reconnaissance response. A summary of the point load strength index results, as well as estimated uniaxial compressive strengths (UCS) calculated using a relationship proposed by Kohno and Maeda (2018), is provided in Online Resource 7. The resulting UCS values indicate that the ultramafic rock and diorite have low strength values based on the Unified Rock Classification System (Keaton and DeGraff 1996).

The bedrock within the head scarp area is generally highly fractured and weathered. A smooth bedrock surface is present in the western portion of the head scarp (Fig. 1f) with an average orientation of 292°/45° (strike [right-hand rule—RHR]/dip). Based on analysis of 159 structural measurements (see Fig. 5b for locations), the bedrock contains five major joint sets (JS) that have similar trends to the mapped lineament sets (LS) (see Online Resources 3 and 8 for more information). For example, the two lineaments that cross the head of the BRLS (Fig. 5b) have trends of 113°/293° (northern) and 108°/288° (southern), corresponding to the average orientation of one JS and to the measurements of the planar bedrock surface exposed in the head scarp. A third prominent lineament forms the left (west) flank of the BRLS head and has a trend of 177°/357°, which is part of one LS and similar in orientation to another JS.

Change detection

We conducted a change detection analysis between 2014 and 2021 lidar epochs. Assuming spatially uniform errors and using the square root of the sum of squares approach to calculate the error propagated into the DEM of difference (DoD) (Wheaton et al. 2010), the resulting minimum level of detection (minLoD) is 0.047 m. Observations of the 2014 3D point cloud, however, revealed a low point density with only one or two points per m^2 in areas of dense tree canopy. This resulted in apparent vertical differences in areas that were presumably stable. Thus, we chose a conservative approach, masking all differences to ± 0.5 m. We converted the DoD raster to ASCII format to quantify areas of vertical change and thus calculate the change in volume. Figure 5c contains the results of the 2014–2021 change detection, with approximately 134,300 m^3 of material loss in the landslide head region. This area of significant volume loss corresponds well with the identified PLS source area

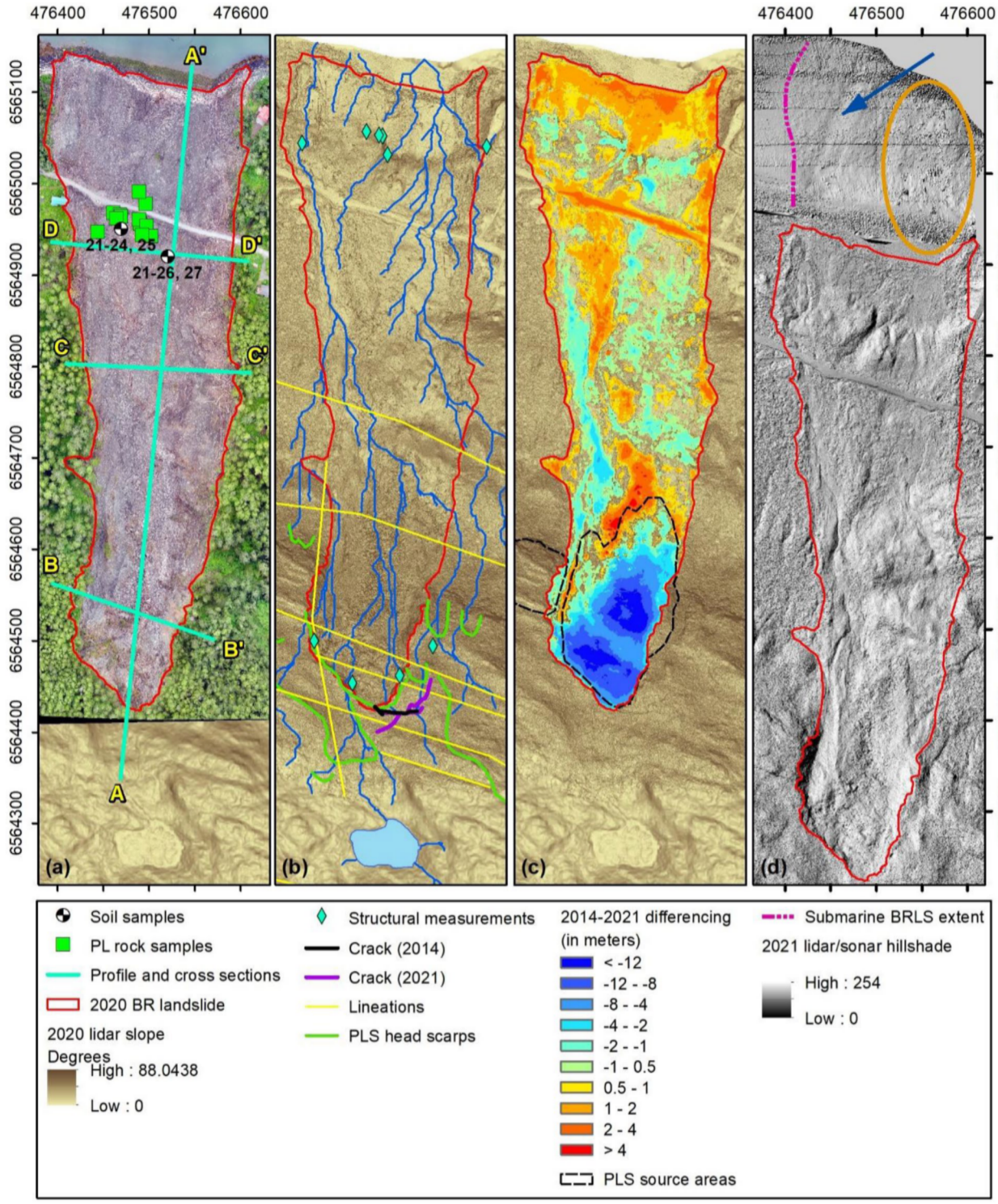

Fig. 5 Beach Road Landslide (BRLS): (**a**) 2021 optical imagery of slide extent, soil and rock sample locations, and profile locations; (**b**) geologic features and hydrology; (**c**) change detection results from 2014 to 2021 lidar epochs; (**d**) subaerial and submarine landslide extents (dark blue arrow points to submarine channel, and orange oval indicates area of boulder deposition). Panels (**a**)–(**c**) share the same extent, as indicated in (**a**); all panels are 1:6,500. Base imagery is slope derived from 2020 lidar (Daanen et al. 2021) in (**a**)—(**c**), and 2021 lidar in (**c**) and (**d**)

from the 2014 lidar (see dashed black line in Fig. 5c). There was approximately 52,800 m^3 of deposition throughout the landslide body including trees deposited along the flanks, with a total landslide volume of about 187,100 m^3. The discrepancy between volume displaced and volume deposited indicates that the majority of the landslide debris (or roughly 81,500 m^3) entered the inlet. Figure 5d is a combination of hillshades from the 2021 subaerial lidar data and the submarine sonar data. The E-W trending lines in the sonar data are artifacts of data collection and processing; thus, we use these data for qualitative purposes only. The dashed pink line indicates the interpreted western extent of the debris flow path based on change in roughness. To the east, we interpret an area of boulders deposited by the BRLS (indicated by the orange oval). The eastern extent is not definable in the sonar data. Additionally, the inlet floor becomes much deeper to the north, making the full extent of the submarine deposit undefinable using these data. The dark blue arrow in Fig. 5d indicates a prominent submarine channel. This channel may represent the northern extent of the N-S trending lineament that forms the eastern portion of the head scarp.

The high-resolution of the 2021 lidar data and imagery allows a more thorough analysis of the areas of change. Online Resource 9 contains examples of areas that may have gone unnoticed with lower-resolution data, including areas of bedrock scour and debris deposition during sluggish flow after the landslide event, a large boulder field, and the crack area uphill and to the east of the head scarp. Focusing on the crack area, the DoD indicates that the ground surface between the crack and the head scarp dropped up to 1.4 m. We mapped the main E-W trending crack as 48.5-m long in the 2014 lidar. The 2021 lidar data and field measurements indicate that the length of this crack increased to 53.4 m. Additionally, in 2021 we mapped a second NE-SW trending crack that roughly paralleled the head scarp and was 82.4 m long.

Discussion and conclusions

Why did this landslide occur here? Landslides have a higher likelihood of occurring in areas of previous landslide activity (e.g., Highland and Bobrowsky 2008). The geomorphic analysis of the area indicates that much of the north side of Riley Ridge has experienced landslide events, as evident through paleo-head scarps and displaced masses of rock. The source material of the 2020 BRLS was visible in lidar collected before the event. The geomorphic analysis also points to significant structural features in the bedrock that defined the head scarp area, indicating that the slide initiated as a planar failure along what is likely a fault plane paralleling the prominent E-W trending lineaments. The intersection of the N-S trending lineament (also likely a fault) with the failure plane provided the detachment necessary to form the source area. This N-S trending fault may form the left (west) flank of the BRLS and extend into the ocean, as indicated by the sonar data. The rock itself is weak and easily disintegrates. Once in motion, the moving rock mass quickly pulverized and incorporated additional water, becoming a debris flow. The velocities of subsequent movement after the first major event (i.e., 1.6 m s^{-1}) and of the debris flood (i.e., 5.5 m s^{-1}) determined from video analysis provide data points that can inform future debris flow studies, since velocities are typically back-calculated after the debris flow occurs (Prochaska et al. 2008; Theule et al. 2018).

We consider the tremendous amount of water resulting from rainfall and snowmelt during the AR as the trigger of the BRLS. The pond near the crest of the ridge served as a reservoir, collecting rainfall and snowmelt to produce a concentrated flow through its outlet stream. Water draining from the pond flowed into the prominent crack at the head scarp (and likely into a network of fractures in the head scarp area), increasing the pore water pressure and lowering the effective stress on the failure plane, thus facilitating the initial movement of the rock debris. In contrast, the watershed areas above PLS 2 and 3 do not have similar reservoirs. Additionally, we did not observe any cracks in the lidar above the paleo-head scarps for PLS 2 and 3, suggesting that more of the runoff during the 2020 AR event may have remained as surface flow. These factors may have contributed to why the PLS 1 area formed the BRLS, whereas PLS 2 and 3 did not form similar landslides.

This study illustrates the importance of mapping pre-existing landslide features on the landscape. Identifying areas such as the PLS source areas is critical, as these are likely to form future landslide events. In addition, understanding discontinuities within the bedrock and its strength properties can inform the likelihood of future landslide occurrence. More critical is the vertical displacement in the mass of rock between the crack and the head scarp of the BRLS, and the lengthening of the crack system observed between 2014 and 2021. The removal of the PLS source area during the 2020 BRLS effectively debuttressed this rock mass, making it especially vulnerable during future heavy precipitation events.

Lifelong residents of the Haines area indicated that winter storms are not new; however, the heavy rainfall instead of snowfall is unusual (Godinez 2020). Annual precipitation trends across Southeast Alaska from 1969 to 2018 demonstrate increases ranging from 4.7% to 15.1% (Thoman and Walsh 2019). Modeling future climate using the RCP8.5 emissions scenario, Lader et al. (2020) projected that Southeast Alaska will experience a temperature increase of 1°–3 °C depending on the season, with increased precipitation in fall and winter. This points to warmer and wetter winters, with a potential increase in ROS events. Continued warming also is expected to increase the number of ARs that impact North America's west coast (Sharma and Déry 2020). ROS events typically occur in late autumn/early winter and are frequently associated with ARs, relating to an increase in flood risk and, in turn, landslides (Sharma and Déry 2020). With each AR, the risk of landslide activity in the affected area is renewed, particularly if soils are already saturated from prior rainfall events.

As the likelihood of extreme precipitation events increases, so should the instrumentation necessary to inform the risk of flooding or landslides. Instrumentation at multiple locations at high elevations reporting a full suite of meteorological, hydrological, and soil information is vital for thoroughly analyzing weather events. Therefore, we recommend the development of an AR scale for Southeast Alaska, similar to what Ralph et al. (2019) developed for the west coast of the USA, but also coupled with geological information. Such a coupled system could enhance warnings to residents in landslide-prone areas when a strong AR or significant ROS event is on the horizon.

The high-resolution lidar and imagery of the BRLS produced in this study will serve as excellent post-landslide data from which subsequent epochs can be differenced. Future work may include how the bare landslide surface evolves with time, including the

establishment of vegetation, and how the landslide debris affected and transformed the beach environment. We recommend additional analysis of high-resolution lidar imagery throughout the Haines area and other areas of Southeast Alaska, where the dynamic geologic history produces beautiful scenery and lush forests that hide the potential geohazards. Identifying areas of previous landslide activity and factors that contribute to landslide events are important steps in reducing landslide impacts on communities (Wisher 1998). The interpreted PLS source areas and extents identified in this study should be confirmed through field investigations, including subsurface explorations and tree coring, where practical. With the aid of the map produced from this study, we recommend targeted sampling of the paleo-shorelines, and collecting and dating additional shell fragments to fine-tune the relationship between elevation and age. Particular attention should be paid to the uplifted shorelines between sea level and 10 m asl to establish any effects of GIA from the LIA in the area. Finally, we recommend investigation of the prominent cliff along the north shore of the AOI to determine the nature of its formation, as it may inform hazard analysis of the Haines area.

Acknowledgements

This material is based upon work supported by the National Science Foundation (NSF) under Grant No. 2114015. Any opinions, findings, and conclusions or recommendations expressed in this material are those of the authors and do not necessarily reflect the views of the NSF. The authors thank: R. Daanen, A. Willingham, J. Norton, D.A. Stevens, and C. Maio for data, field observations, and advice and guidance. The authors also thank the residents of Haines for their generosity and support, with special thanks to L. Cornejo, E. Stevens, T. Eckhoff, C. Wooten, A. Fullerton, W. Slate, R. White, M. and M. Balise, D. Geason, T. Ganner, M. Hunter, J. Messano, G. and K. Keller, and the Andriesen family.

Funding

Funding was acquired by M. M. Darrow. Data collection and analysis were performed by M. M. Darrow, V. A. Nelson, M. Grilliot, and J. Wartman. The first draft of the manuscript was written by M. M. Darrow, and all authors read and approved the final manuscript.

Declarations

Conflict of interest The authors have no conflicts of interest associated with this manuscript. Lidar data from 2014 and 2020 are available through the DGGS web portal (https://elevation.alaska.gov/); all other data will be archived in DesignSafe-CI.

Open Access This article is licensed under a Creative Commons Attribution 4.0 International License, which permits use, sharing, adaptation, distribution and reproduction in any medium or format, as long as you give appropriate credit to the original author(s) and the source, provide a link to the Creative Commons licence, and indicate if changes were made. The images or other third party material in this article are included in the article's Creative Commons licence, unless indicated otherwise in a credit line to the material. If material is not included in the article's Creative Commons licence and your intended use is not permitted by statutory regulation or exceeds the permitted use, you will need to obtain permission directly from the copyright holder. To view a copy of this licence, visit http://creativecommons.org/licenses/by/4.0/.

References

Alaska Department of Natural Resources (ADNR) (2021) Open Data Portal. ADNR. https://data-soa-dnr.opendata.arcgis.com/search?collection=Dataset&tags=Physical. Accessed 20 Sep 2021

Ayalew L, Yamagishi H, Marui H, Kanno T (2005) Landslides in Sado Island of Japan: part I. case studies, monitoring techniques and environmental considerations. Eng Geol 81:419–431. https://doi.org/10.1016/j.enggeo.2005.08.005

Baichtal JF, Lesnek AJ, Carlson RJ, Schmuck NS, Smith JL, Landwehr DJ, Briner JP (2021) Late Pleistocene and early Holocene sea-level history and glacial retreat interpreted from shell-bearing marine deposits of southeastern Alaska, USA. Geosphere 17(6):1590–1615. https://doi.org/10.1130/GES02359.1

Brew DA, Ford AB (1994) The Coast Mountains Plutonic-Metamorphic Complex and Related Rocks between Haines, Alaska, and Fraser, British Columbia – Tectonic and Geologic Sketches and Klondike Highway Road Log: U.S. Geological Survey Open-File Report 94–268, 25 p

Brideau M-A, Sturzenegger M, Stead D, Jaboyedoff M, Lawrence M, Roberts NJ, Ward BC, Millard TH, Clague JJ (2012) Stability analysis of the 2007 Chehalis lake landslide based on long-range terrestrial photogrammetry and airborne LiDAR data. Landslides 9:75–81. https://doi.org/10.1007/s10346-011-0286-4

Brothers DS, Elliott JL, Conrad JE, Haeussler PJ, Kluesner JW (2018) Strain partitioning in Southeastern Alaska: is the Chatham Strait Fault active? Earth Planet Sci Lett 481:362–371. https://doi.org/10.1016/j.epsl.2017.10.017

Cacek CC (1989) The relationship of mass wasting to timber harvest activities in the Lightning Creek basin, Idaho and Montana. MS Thesis, Eastern Washington University

Cardinali M, Ardizzone F, Galli M, Guzzetti F, Reichenbach P (1999) Landslides triggered by rapid snow melting: the December 1996-January 1997 event in Central Italy. Proc., EGS Plinius Conference, Maratea, Italy, October 1999, 439–448

Carrara PE, Ager TA, Baichtal JF (2007) Possible refugia in the Alexander Archipelago of southeastern Alaska during the late Wisconsin glaciation. Canadian Journal of Earth Science 44(2):229–244. https://doi.org/10.1139/E06-081

Coe JA, Baum RL, Allstadt KE, Kochevar BF Jr, Schmitt RG (2016) Rock-avalanche dynamics revealed by large-scale field mapping and seismic signals at a highly mobile avalanche in the West Salt Creek valley, western Colorado. Geosphere 12(2):607–631. https://doi.org/10.1130/GES01265.1

Contreras TA, Sarikhan I, Polenz M, Powell J, Skov R (2009) Collecting, analyzing and sharing large volumes of digital photos during geological disasters; methods developed from landslide reconnaissance flights following the January 2009 storm in western Washington State. Abstracts with Programs, Geological Society of America 41(7):136

Cwynar LC (1990) A late Quaternary vegetation history from Lily Lake, Chilkat Peninsula, southeast Alaska. Can J Bot 68:1106–1112

Daanen RP, Herbst AM, Wilstrom Jones K, Wolken GJ (2021) High-resolution lidar data for Haines, Southcentral Alaska, December 8–12, 2020. Alaska Division of Geological & Geophysical Surveys Raw Data File 2021–4, 8 p. https://doi.org/10.14509/30595

Davis A, Plafker G (1985) Comparative geochemistry and petrology of Triassic basaltic rocks from the Taku terrane on the Chilkat Peninsula and Wrangellia. Canadian Journal of Earth Science 22:183–194

DeGraff JV (2001) Sourgrass debris flow; a landslide triggered in the Sierra Nevada by the 1997 New Year storm. In Ferriz, H. and Anderson, R. (Eds.), Special Publication – Association of Engineering Geologists, 12: 69–76

Evans SG (2002) Derailments due to landslides and geotechnical failure in Canada's railway system. Abstracts with Programs, Geological Society of America 34(6):90

Evans SG, Clague JJ (1999) Rock avalanches on glaciers in the Coast and St. Elias Mountains, British Columbia. Proc., 13th Annual Vancouver Geotechnical Society Symposium, May 28, 1999, 115–123

Godinez C (2020) Changing climate means more landslides in future, scientists say in wake of Haines disaster. Chilkat Valley News. Available from: https://www.chilkatvalleynews.com/story/2020/12/03/news/changing-climate-means-more-landslides-in-future-scientists-say-in-wake-of-haines-disaster/14427.html. Accessed on 9 Dec 2020

Guthrie RH, Mitchell SJ, Lanquaye-Opoku N, Evans SG (2010) Extreme weather and landslide initiation in coastal British Columbia. Q J Eng Geol Hydrogeol 43:417–428. https://doi.org/10.1144/1470-9236/08-119

Highland LM, Bobrowsky P (2008) The Landslide Handbook – A Guide to Understanding Landslides. U.S. Geological Survey Circular 1325, 129 p. https://doi.org/10.3133/cir1325

Himmelberg GR, Loney RA (1995) Characteristics and Petrogenesis of Alaskan-Type Ultramafic-Mafic Intrusions, Southeastern Alaska. U.S. Geological Survey Professional Paper 1564, 51 p

Hungr O, Evans SG, Bovis MJ, Hutchinson JN (2001) A review of the classification of landslides of the flow type. Environ Eng Geosci 7(3):221–238

Kanan R (2016) Rain, rain and more rain. National Weather Service, National Oceanic and Atmospheric Administration. Available at https://www.weather.gov/media/ajk/articles/rain.pdf. Accessed on Nov 25, 2021

Kaufman DS, Young NE, Briner JP, Manley WF (2011) Alaska Palaeo-Glacier Atlas (Version 2). In Ehlers, J. and Gibbard, P. L. (eds.), Quaternary Glaciations Extent and Chronology, Part IV: A Closer Look. Developments in Quaternary Science 15, Amsterdam, Elsevier, 427–445

Keaton JR, DeGraff JV (1996) Surface observation and geologic mapping. In Turner, A.K., and Schuster, R.L., Eds., Landslides: Investigation and Mitigation. Special Report 247, Trans Res Board 178–230

Kohno M, Maeda H (2018) Estimate of uniaxial compressive strength of hydrothermally altered soft rocks based on strength index tests. Geomaterials 8:15–25. https://doi.org/10.4236/gm.2018.82002

Lader R, Bidlack A, Walsh JE, Bhatt US, Bieniek PA (2020) Dynamical downscaling for Southeast Alaska: historical climate and future projections. J Appl Meteorol Climatol 59(10):1607–1623. https://doi.org/10.1175/JAMC-D-20-0076.1

Larsen CF, Motyka RJ, Freymueller JT, Echelmeyer KA, Ivins ER (2005) Rapid viscoelastic uplift in southeast Alaska caused by post-Little Ice Age glacial retreat. Earth Planet Sci Lett 237:548–560. https://doi.org/10.1016/j.epsl.2005.06.032

Larsen PH, Goldsmith S, Smith O, Wilson ML, Strzepek K, Chinowsky P, Saylor B (2008) Estimating future costs for Alaska public infrastructure at risk from climate change. Glob Environ Chang 18(3):442–457. https://doi.org/10.1016/j.gloenvcha.2008.03.005

Lemke RW, Yehle LA (1972) Reconnaissance engineering geology of the Haines area, Alaska, with emphasis on evaluation of earthquake and other geologic hazards: U.S. Geological Survey Open-File Report 72–229, 109 p., 2 sheets, scale 1:24,000

Lesnek AJ, Briner JP, Baichtal JF, Lyles AS (2020) New constraints on the last deglaciation of the Cordilleran Ice Sheet in coastal Southeast Alaska. Quatern Res 96:140–160. https://doi.org/10.1017/qua.2020.32

MacKevett Jr. EM, Robertson EC, Winkler GR (1974) Geology of the Skagway B-3 and B-4 Quadrangles, Southeastern Alaska: U.S. Geological Survey Professional Paper 832, 33 p

Manley WF, Kaufman DS (2002) Alaska PaleoGlacier Atlas: Institute of Arctic and Alpine Research (INSTAAR), University of Colorado, instaar.colorado.edu/QGISL/ak_paleoglacier_atlas, v. 1

MesoWest (2020) Observations and Summaries: University of Utah. Available from: https://mesowest.utah.edu/. Accessed on 7 Dec 2020

Motyka RJ, Larsen CF, Freymueller JT, Echelmeyer KA (2007) Post Little Ice Age rebound in the Glacier Bay Region. In Piatt, J.F. and Gende, S.M., Eds., Proceedings of the Fourth Glacier Bay Science Symposium, October 26–28, 2004: US Geol Surv Sci Investig Rep 2007–5047:57–59

National Water and Climate Center (NWCC) (2021) Report generator 2.0. USDA Natural Resources Conservation Service. Available from: https://wcc.sc.egov.usda.gov/reportGenerator/releaseNotes. Accessed on 29 Nov 2021

National Weather Service (NWS) (2021a) Hydrometeorological design studies center precipitation frequency data server (PFDS). National Oceanic and Atmospheric Administration. Available from: https://hdsc.nws.noaa.gov/hdsc/pfds/pfds_map_ak.html. Accessed 26 Nov 2021a

National Weather Service (NWS) (2021b) NOWData – NOAA Online Weather Data. National Oceanic and Atmospheric Administration. Available from: https://www.weather.gov/arh/climate?wfo=ajk. Accessed on 25 Nov 2021

Naudet V, Lazzari M, Perrone A, Loperte A, Piscitelli S, Lapenna V (2008) Integrated geophysical and geomorphological approach to investigate the snowmelt-triggered landslide of Bosco Piccolo village (Basilicata, southern Italy). Eng Geol 98(3–4):156–167. https://doi.org/10.1016/j.enggeo.2008.02.008

Quantum Spatial, Inc. (QSI) (2014) Skagway, Haines, and Petersburg LiDAR: technical data report: QSI, 36 p. Available from https://elevation.alaska.gov/

Perica S, Kane D, Dietz S, Maitaria K, Martin D, Pavlovic S, Roy I, Stuefer S, Tidwell A, Trypaluk C, Unruh D, Yekta M, Betts E, Bonnin G, Heim S, Hiner L, Lilly E, Narayanan J, Yan F, Zhao T (2012) NOAA Atlas 14: Precipitation-Frequency Atlas of the United States, v. 7, vers. 2, Alaska. National Oceanic and Atmospheric Administration and University of Alaska Fairbanks, 119 p. https://www.weather.gov/media/owp/oh/hdsc/docs/Atlas14_Volume7.pdf

Plafker G, Blome CD, Silberling NJ (1989) Reinterpretation of lower Mesozoic rocks on the Chilkat Peninsula, Alaska, as a displaced fragment of Wrangellia. Geology: 17(1):3–6. https://doi.org/10.1130/0091-7613(1989)017<0003:ROLMRO>2.3.CO;2

Prochaska AB, Santi PM, Higgins JD, Cannon SH (2008) A study of methods to estimate debris flow velocity. Landslides 5:431–444. https://doi.org/10.1007/s10346-008-0137-0

Ralph FM, Rutz JJ, Cordeira JM, Dettinger M, Anderson M, Reynolds D, Schick LJ, Smallcomb C (2019) A scale to characterize the strength and impacts of atmospheric rivers. Bull Am Meteor Soc 100(2):269–289. https://doi.org/10.1175/BAMS-D-18-0023.1

Sharma AR, Déry SJ (2020) Contribution of atmospheric rivers to annual, seasonal, and extreme precipitation across British Columbia and southeastern Alaska. J Geophys Res Atmos. https://doi.org/10.1029/2019JD031823

State of Alaska (SOA) (2021) Open Data Geoportal. SOA. https://gis.data.alaska.gov/pages/Imagery%20Program. Accessed 29 Oct 2021

Theule JI, Crema S, Marchi L, Cavalli M, Comiti F (2018) Exploiting LSPIV to assess debris-flow velocities in the field. Nat Hazards Earth Syst Sci 18:1–13. https://doi.org/10.5194/nhess-18-1-2018

Thoman R, Walsh JE (2019) Alaska's changing environment: documenting Alaska's physical and biological changes through observations. International Arctic Research Center, University of Alaska Fairbanks. Available from https://uaf-iarc.org/our-work/alaskas-changing-environment/. Accessed on 25 Dec 2019

Weather Bureau (2005) Storm Data. U.S. Weather Bureau. Available from https://books.google.com/books?id=PoaQUEKivqkC&dq=2005+november+alaska+storm+landslide&source=gbs_navlinks_s. Accessed on 14 Dec 2021

Western Regional Climate Center (WRCC) (2021) Climate of Alaska. WRCC. Available from: https://wrcc.dri.edu/Climate/narrative_ak.php. Accessed 26 Nov 2021

Wheaton JM, Brasington J, Darby SE, Sear DA (2010) Accounting for uncertainty in DEMs from repeat topographic surveys: improved sediment budgets. Earth Surf Process Landf 35:136-156. https://doi.org/10.1002/esp.1886

Wilson FH, Hults CP, Mull CG, Karl SM (2015) Geologic Map of Alaska: U.S. Geological Survey Scientific Investigations Map 3340, 196 p., 2 sheets, scale 1:1,584,000, https://alaska.usgs.gov/science/geology/state_map/interactive_map/AKgeologic_map.html

Wisher AP (1998) Factors contributing to landslide activity in the winter of 1995–96, Clearwater County near Orofino, Idaho. Geol Soc Am Abstr Programs 30(7):144

Supplementary Information The online version contains supplementary material available at https://doi.org/10.1007/s10346-022-01899-3.

Margaret M. Darrow (✉) · **Victoria A. Nelson**
Dept. of Civil, Geological, and Environmental Engineering, University of Alaska Fairbanks, Fairbanks, Alaska, USA
Email: mmdarrow@alaska.edu

Michael Grilliot
Natural Hazard and Disaster Reconnaissance (RAPID) Facility, Dept. of Civil and Environmental Engineering, University of Washington, Seattle, WA, USA

Joseph Wartman
Dept. of Civil and Environmental Engineering, University of Washington, Seattle, WA, USA

Aaron Jacobs
National Weather Service Juneau Forecast Office, National Oceanic and Atmospheric Administration, Juneau, Alaska, USA

James F. Baichtal
Tongass National Forest, Thorne Bay, Alaska, USA

Cindy Buxton
Lynn Canal Geological Services, Haines, Alaska, USA